

Research Paper

Glucose Oxidase-Instructed Traceable Self-Oxygenation/Hyperthermia Dually Enhanced Cancer Starvation Therapy

Ting He^{1,2*}, Han Xu^{1*}, Yifan Zhang¹, Shijian Yi³, Run Cui¹, Shaojun Xing¹, Chaoliang Wei¹, Jing Lin¹, Peng Huang¹✉

1. Marshall Laboratory of Biomedical Engineering, International Cancer Center, Laboratory of Evolutionary Theranostics (LET), School of Biomedical Engineering, Shenzhen University Health Science Center, Shenzhen 518060, China.
2. Key Laboratory of Optoelectronic Devices and Systems of Ministry of Education and Guangdong Province, College of Optoelectronic Engineering, Shenzhen University, Shenzhen 518060, China.
3. Department of General Surgery, Shenzhen University General Hospital, Shenzhen 518055, China.

*These authors contributed equally to this work.

✉ Corresponding author: Peng Huang, 1066 Xueyuan Boulevard Shenzhen University Health Science Center, Shenzhen, 518060, China. E-mail: peng.huang@szu.edu.cn (Peng Huang).

© The author(s). This is an open access article distributed under the terms of the Creative Commons Attribution License (<https://creativecommons.org/licenses/by/4.0/>). See <http://ivyspring.com/terms> for full terms and conditions.

Received: 2019.09.18; Accepted: 2019.11.04; Published: 2020.01.01

Abstract

Cancer theranostics based on glucose oxidase (GOx)-induced starvation therapy has got more and more attention in cancer management. Herein, GOx armed manganese dioxide nanosheets (denoted as MNS-GOx) were developed as cancer nanotheranostic agent for magnetic resonance (MR)/photoacoustic (PA) dual-modal imaging guided self-oxygenation/hyperthermia dually enhanced starvation cancer therapy. The manganese dioxide nanomaterials with different morphologies (such as nanoflowers, nanosheets and nanowires) were synthesized by a biomimetic approach using melanin as a biotemplate. Afterwards, the manganese dioxide nanosheets (MNS) with two sides and large surface area were selected as the vehicle to carry and deliver GOx. The as-prepared MNS-GOx can perform the circular reaction of glucose oxidation and H₂O₂ decomposition for enhanced starvation therapy. Moreover, the catalytic activity of GOx could be further improved by the hyperthermia of MNS-GOx upon near-infrared laser irradiation. Most intriguingly, MNS-GOx could achieve “turn-on” MR imaging and “turn-off” PA imaging simultaneously. The theranostic capability of MNS-GOx was evaluated on A375 tumor-bearing mice with all tumor elimination. Our findings integrated molecular imaging and starvation-based synergistic cancer therapy, which provided a new platform for cancer nanotheranostics.

Key words: manganese oxidase, melanin, photothermal therapy, starvation therapy, synergistic therapy.

Introduction

Glucose is an important source of energy in living organisms, the occurrence and development of many diseases are closely related to the glucose metabolism¹⁻². Utilization of glucose oxidation through the catalytic reaction of glucose oxidase (GOx) can cut off energy supply to inhibit the tumor growth³⁻⁵, which are known as GOx-based starvation therapy that has attracted more and more attention in cancer management in recent years^{4, 6-11}. However, the

starvation therapies based on GOx are restricted by the hypoxic state of tumor tissues, because glucose oxidation reactions need a large amount of oxygen (O₂)¹²⁻¹³. Therefore, how to improve the O₂ level of tumor tissues will directly decide the therapeutic effect of GOx-based starvation therapy.

The products of glucose oxidation are including gluconic acid and hydrogen peroxide (H₂O₂). Meanwhile, tumor microenvironments also contain a

high content of H_2O_2 . As we know, the decomposition of H_2O_2 can produce water and O_2 , thus promising the melioration of tumor hypoxia. Manganese oxide (MnO_2) nanomaterials can catalyze decomposition reaction to produce O_2 to modulate solid tumor hypoxia for effective starvation therapy¹⁴⁻¹⁸. Therefore, the combination of MnO_2 and GOx will accelerate glucose consumption to improve the starvation therapeutic effect. Recently, MnO_2 -based theranostic agents have been widely explored^{14,19-23}, such as urchin-shaped MnO_2 nanoparticles^{17, 24-25}, hollow MnO_2 nanoplateform²⁶⁻²⁷, MnO_2 nanosheets²⁸⁻³¹ and Mn-based layered double hydroxide³² and so on. However, most of MnO_2 nanomaterials need polyethylene glycol (PEG) modification to improve their biocompatibility and water solubility²⁸. Melanin, an endogenous biomolecule, has been employed as coating materials to endow nanoplateforms with good biocompatibility, dispersibility, and strong near-infrared (NIR) absorption³³⁻³⁷. Moreover, melanin-based nanoplateforms have great potential in the biomedical applications of photoacoustic imaging (PAI) and photothermal therapy (PTT).

Herein, we used melanin as the biotemplate to directly synthesize MnO_2 nanomaterials with different morphologies (such as nanoflowers, nanosheets and nanowires). The melanin coated MnO_2 have good biocompatibility and strong NIR absorption. Afterwards, GOx armed manganese dioxide nanosheets (denoted as MNS-GOx) were explored for cancer nanotheranostics with following characteristics (Scheme 1): (i) the circular reaction of glucose oxidation and H_2O_2 decomposition; (ii) the enhancement of catalytic

activity of GOx by the hyperthermia of MNS-GOx; (iii) activatable magnetic resonance (MR)/photoacoustic (PA) dual-modal imaging. The theranostic capability of MNS-GOx was carefully investigated both *in vitro* and *in vivo*. The as-prepared MNS-GOx has great potential in traceable cancer therapy, especially for MR/PA dual-modal imaging guided self-oxygenation/hyperthermia dually enhanced starvation cancer therapy.

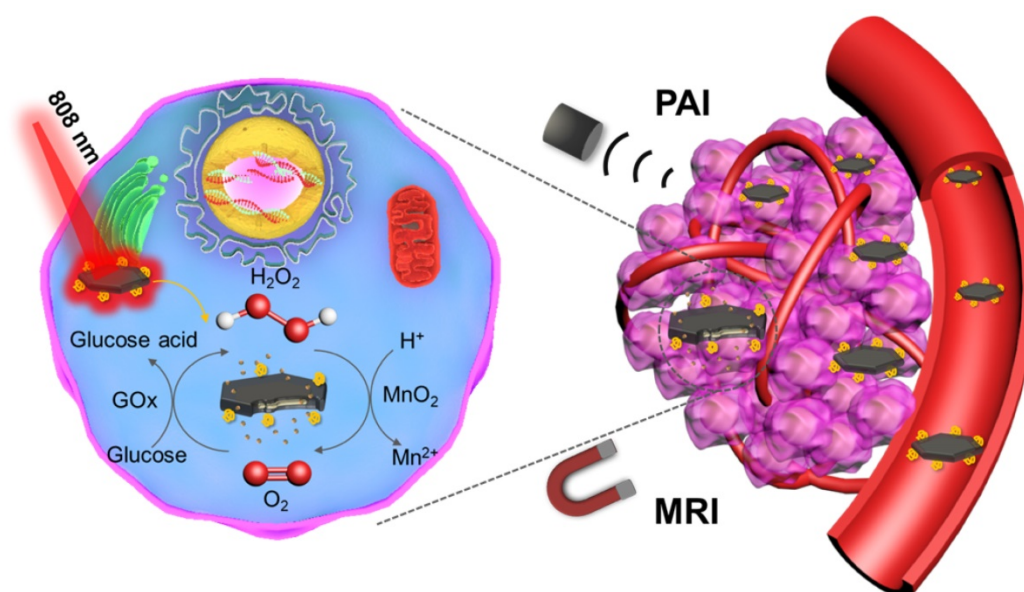
Experimental Section

Synthesis of MNS

MnO_2 nanosheets (MNS) were synthesized by the biomimetic synthesis method using melanin as the biomimetic template. Typically, 0.4 mL melanin (2 mg/mL) and 3.2 mL ethanol were added into 48 mL deionized (DI) water. The pH value of the mixed solution was adjusted to 7.4~7.8. Then the solution was heated to 90 °C, 0.32 mL potassium permanganate ($KMnO_4$) (0.05 M) was slowly added under vigorous stirring. The system was kept stirring for 30 min at 90 °C. The product was purified and concentrated by an ultrafilter (30 kDa).

Synthesis of MNS-GOx

GOx was conjugated on the surface of MNS through the 1-(3-Dimethylaminopropyl)-3-ethylcarbodiimide hydrochloride (EDC)/N-Hydroxysuccinimide (NHS) reaction between carboxyl groups of MNS and amine groups of GOx. In brief, 10 mg EDC and 5 mg NHS were added into 4 mL MNS (1 mg/mL). After 2 h, 40 μ L GOx (2 mg/mL) was added and the mixture solution was stirred for



Scheme 1. Schematic illustration of MNS-GOx for magnetic resonance (MR)/photoacoustic (PA) dual-modal imaging guided self-oxygenation/hyperthermia dually enhanced starvation cancer therapy.

another 8 h. The MNS-GOx was washed with DI water for several times and suspended in water for further use. In further experiments, the ratios of 200:1 and 1:1 of MNS: GOx were prepared for *in vitro* and *in vivo* experiments, respectively.

Characterization

The morphologies of MnO₂ nanomaterials were observed by high-resolution field emission transmission electron microscope (TEM) (JEM-3200FS, JEOL, Japan). The thickness of MNS was measured by atom force microscope (AFM) (MultiMode 8, Bruker, Germany). X-ray diffraction (XRD) pattern of MNS was detected by X-ray diffractometer (D8 Advance, Bruker, Germany). Dynamic light scattering (DLS) and Zeta potential was measured on Zetasizer Nano-ZS90 (Malven, England). Fourier-transform infrared (FT-IR) spectra were collected on a FT-IR spectrometer (Spectrum Two, PerkinElmer, USA). UV/Vis absorption spectra were measured on a Cary 60 UV/Vis spectrophotometer (Agilent Technologies, Santa Clara, CA, USA). The Mn element concentration of MNS was quantified by an inductively coupled plasma-atomic emission spectrometry (ICP-AES) (JY 2000-2, Horiba, France).

pH-Responsive Degradations of MNS and MNS-GOx

The pH-responsive degradations of MNS and MNS-GOx were monitored by UV/Vis spectrophotometer. The optical density (OD) at 400 nm of MNS (100 µg/mL) or MNS-GOx (100 µg/mL) in PBS solutions (5 mM glucose, pH 7.4) was measured over time. Additionally, 4 mL of MNS (100 µg/mL) or MNS-GOx (100 µg/mL) was loaded into a dialysis bag with the molecular weight cut-off of 3500 Da. Then the bag was immersed into 50 mL of buffer solutions with different pH values (5 mM glucose pH 5.0, 6.0, 7.4) under vigorous stirring at room temperature. At different time points, 2 mL of buffer solution was taken out and the released Mn²⁺ was detected by ICP-AES. Meanwhile, an isometric buffer solution was added to keep the total volume same.

Photothermal Performance of MNS

The aqueous solutions of MNS (0~200 µg/mL) were stored in Eppendorf tubes, and exposed to 808 nm laser at power density of 1 W/cm² for 3 min. The photothermal stability of MNS (200 µg/mL) were irradiated upon different laser power density of 1 W/cm² for four on/off cycles (on: 2 min, off: 6 min). Real-time thermal imaging was recorded by a SC300 infrared camera (FLIR, Arlington, VA) and quantified by FLIR Examiner software.

T₁ Relaxivity of MNS and MNS-GOx

MNS and MNS-GOx with different Mn element concentration (0.2, 0.4, 0.6, 0.8, 1.0 mM) were dispersed in PBS solutions with different pH values (5, 6, 7.4) for 4 h. Then the T₁ relaxivity was detected by a 3 T clinical MRI scanner (UMR 790, United-Imaging, Shanghai, China). An fast spin echo (FSE) sequence with 19 different values of T₁ (TR (repetition time)=5000 ms; TE (echo time) =100, 150, 200, 250, 300, 350, 400, 450, 500, 550, 600, 700, 800, 900, 1000, 1200, 1300, 1500, 2000 ms) for T₁ measurements. T₁ relaxation times were calculated by fitting the signal intensities with increasing T₁ to $I_{(t)}=I_0[1-k \cdot \exp(-t/T_1)]$ by using a nonlinear least-squares fit of the Levenberg-Marquardt algorithm.

Catalytic Activity of GOx

30 µL of MNS-GOx (1 mg/mL) or GOx (1 mg/mL) was added into 1 mL of glucose solution (30 mM) under oxygen gas flow (5 mL/min). The glucose concentrations were immediately detected by Yuwell 590 glucometer at different time points (0, 2, 4, 6, 8 min). Moreover, the glucose solutions were heated up to 30, 40, 50 or 60 °C. The kinetic parameters (V_{max}) of GOx obtained from the Michaelis-Menten plots at different temperatures³⁸⁻⁴¹. Meanwhile, the catalytic activity of GOx in MNS-GOx was investigated before and after laser irradiation (808 nm laser, 1 W/cm² for 5 min).

In Vitro Synergistic Therapy

For *in vitro* synergistic therapy, four parallel groups were set: control, MNS + laser, MNS-GOx, and MNS-GOx + laser. A375 cells were seeded into a 96-well plate at 10⁴/well and then cultured at 37 °C for 24 h. The cells were incubated with MNS or MNS-GOx (0~1 mM) for 4 h and then exposed to an 808 nm laser at 1 W/cm² for 5 min. Then the old dulbecco's modified eagle medium (DMEM) media were removed and 5 mg/mL 3-(4,5-dimethylthiazol-2-yl)-2,5-diphenyltetrazolium bromide (MTT) in 100 µL DMEM media was added into each well. After co-incubation for another 4 h, the old DMEM media were replaced with 150 µL dimethylsulfoxide (DMSO) per well, and the absorbance at 490 nm was monitored by a microplate reader. The cytotoxicity was finally expressed as the viabilities of different-treated cells in contrast to the untreated control cells.

A375 cells were seeded into a 12-well plate at 7*10⁴/well and then cultured at 37 °C for 24 h. MNS or MNS-GOx (1 mM, DMEM media) was added into each well and co-incubated for 4 h. Then the cells were exposed to an 808 nm laser at 1W/cm² for 5 min. After co-incubation for another 24 h, the cells were

co-stained by Calcein acetoxymethyl ester (calcein AM) and propidium iodide (PI), and then imaged using an Olympus FV1000 fluorescent microscope.

In Vivo MR/PA Dual-Modal Imaging

The tumor-bearing nude mice (~20 g) were intratumoral injected with MNS or MNS-GOx (5 mg/kg). Magnetic resonance imaging (MRI) was performed by a UMR 790 3.0T (United-Imaging, Shanghai, China). T₁-weighted images were acquired by FSE sequence at 0, 0.5, 1, 4, 8, 24 h and the parameters were as follows: TR=700 ms; TE=14.3 ms; Flip Angle=145 °; matrix size, 160 × 160; slice thickness, 1.5 mm. Signal intensities were measured in defined regions of interest (ROI) with software named Image J. The PA images were recorded by a Vevo LAZR2100 system (VisualSonics Inc. New York, NY) equipped with a 40 MHz, 256-element linear array transducer on tumors.

In Vivo Synergistic Therapy

A375 cells were implanted subcutaneously into nude mice (~20 g). *In vivo* treatment was performed when the tumor reached 6 mm in average diameter (10 days after implant). The mice were divided into six groups: PBS as the control group; PBS with laser irradiation (PBS + laser); MNS; MNS-GOx; MNS with laser irradiation (MNS + laser); MNS-GOx with laser irradiation (MNS-GOx + laser). For laser irradiation groups, 808 nm laser with the power of 0.6 W/cm² was used to irradiate tumor tissues for 5 min after intratumoral injection (dose: 5 mg/kg). For each group, the tumor volumes and body weight were measured every two days, and volume of tumors was calculated as (tumor length) × (tumor width/2)². Relative tumor volume was calculated as V/V₀ (V₀ is the tumor volume when the treatment was initiated).

Hemolysis Assay

The red blood cells (RBCs) were isolated from serum by centrifugation of the mixture containing 0.5 mL blood sample and 1 mL PBS solution at 4500 rpm for 3.5 min, then washed the RBCs over five times and diluted the purified cells to 5 mL. Then 0.3 mL volume diluted RBCs suspension was added to quadruple volume of PBS solution with different concentrations of MNS (12.5 to 400 µg/mL). The mixtures were vortexed and kept to stand for 4 h at room temperature. Samples were then centrifuged to measure the absorbance of the supernatants at 541 nm by an UV-vis spectroscopy. RBCs treated with deionized water and PBS were set as positive and negative controls.

Ex vivo Histological Staining

Tumor tissues were collected from

tumor-bearing mice in different groups at day 16 and sectioned into slices for hematoxylin and eosin (H&E) staining. For the toxicity evaluation of MNS or MNS-GOx, mice with intratumoral injection of MNS or MNS-GOx (dose: 5 mg/kg) were sacrificed at day 30 (3 mice per group). Then tumor tissues and major organs (including heart, liver, spleen, lung, kidney and tumor.) were collected, fixed in 10% neutral buffered formalin, embedded in paraffin, cut into 4 µm sections and stained with H&E. Finally, the images of these histological tissue sections were obtained by a BX41 bright field microscopy (Olympus).

Statistical Analysis

Data were presented as mean ± standard deviation (SD). Statistical differences among experimental groups were analyzed using one-way analysis of variance (ANOVA) followed by two-tailed Student's t test. *P* < 0.05 was considered as statistically significant.

Results and Discussions

Preparation and Characterization of MNS and MNS-GOx

MNS were prepared by one-step reduction of KMnO₄ using melanin as a template under neutral conditions, and then modified with GOx by a cross-linker, as shown in **Figure 1A**. Due to an abundant of catechol groups of melanin, it can anchor on the surface of metals oxides⁴². Therefore, the morphologies of MnO₂ were strongly depended on the solubility of melanin under different reaction conditions. The as-prepared MnO₂ nanomaterials were nanoflowers (**Figure 1B**) at acidic condition (pH < 7), ultrathin nanosheets (**Figure 1C**) at neutral condition (pH 7) and nanowires (**Figure 1D**) at alkaline condition (pH 10). The nanoflowers can be formed when the decomposition rate of KMnO₄ was faster in acidic condition and the nanowires were probably formed when the solubility of melanin increased in alkaline solution⁴³. The MNS with two sides and large surface area was chosen as the vehicle to carry and deliver GOx. As shown in **Figure S1**, the hydrodynamic diameter of MNS was about ~70 nm measured by DLS. High resolution TEM image of MNS indicated that the lattice fringe spacing of MNS were 0.232 and 0.288 nm (**Figure S2**), which can be attributed to (311) and (411) according to the XRD pattern (**Figure S3**). EDS spectrum confirmed the high concentration of manganese and oxygen elements in MNS, which is further supported by element mapping images in **Figure S4**. As shown in **Figure S5**, the thickness of MNS was ~2 nm, which indicated the

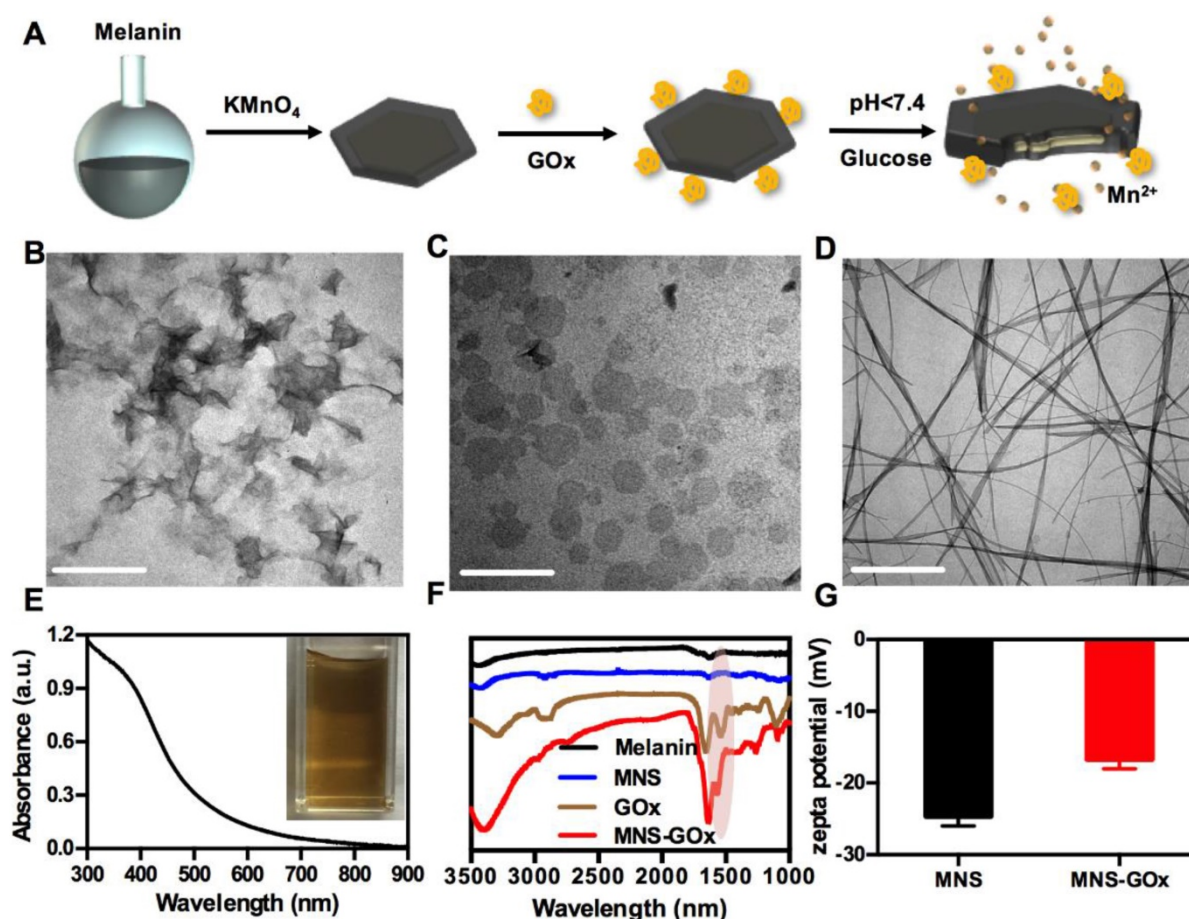


Figure 1. (A) Scheme of the synthesis process of MNS-GOx. TEM images of nanoflowers (B), nanosheets (C), nanowires (D). Scale bar: 200 nm. (E) UV-vis-NIR absorption spectrum of MNS. (F) FT-IR spectra of melanin, MNS, GOx and MNS-GOx. (G) Zeta potentials of MNS and MNS-GOx.

MNS with ultrathin sheet structure.

Melanin as the biotemplate plays an important role in regulating the morphology of MnO_2 nanomaterials during the synthesis process. It can be adsorbed on the surface of MNS through the abundant catechol groups of melanin^{42, 44}. As shown in **Figure 1E**, UV-vis-NIR absorption spectrum of MNS contained the broad absorbance of melanin³⁵ and the characteristic peak of MnO_2 (~400 nm)⁴⁴. The absorbance at 808 nm of MNS was positively correlated with MnO_2 concentration, and the typical equation was $Y = 0.003X + 0.0102$ ($R^2 = 0.9736$) (**Figure S6**). The photothermal effect of MNS exhibited a MNS concentration-dependent under 808 nm laser irradiation (**Figure S7A-C**). After 4 cycles of laser irradiation, MNS still remained its excellent photothermal conversion property, suggested that MNS has a great photostability (**Figure S7D**). The melanin modified MnO_2 had a large number of carboxyls for further surface modification. GOx can be covalently conjugated onto the surface of MNS by EDC/NHS reaction. FT-IR spectrum of MNS-GOx showed a new peak at about 1650 cm^{-1} , indicating that GOx was successfully grafted onto the surface of MNS

(**Figure 1F**). The zeta potentials of MNS and MNS-GOx were -24.6 and -16.7 mV, respectively (**Figure 1G**). These results indicated GOx was successfully loaded by MNS.

pH-Responsive Degradation of MNS-GOx

MnO_2 nanomaterials can be decomposed into Mn^{2+} in the tumor microenvironment for MRI and alleviating the hypoxia of tumor^{24, 28, 45-46}. As shown in **Figure 2A**, the OD at 400 nm of MNS-GOx decreased from 0.70 to 0.17 within 8 h in 5 mM glucose solution, while that of MNS kept stable at about 0.84. Because MNS-GOx can catalyze glucose to produce gluconic acid and H_2O_2 , which promoted the degradation of MNS. The color of MNS-GOx solution was changed from brown to colorless over time (**Figure S8**). Moreover, the quantified concentration of Mn^{2+} released from MNS or MNS-GOx was further verified the degradation of MNS. As shown in **Figure 2B-C**, the Mn^{2+} released from MNS-GOx can reach 89% at pH 5, but it was only 56.3% of MNS at the same condition. The concentration of released Mn^{2+} will directly affect the following longitudinal relaxivity (r_1). Because the released Mn^{2+} had five unpaired

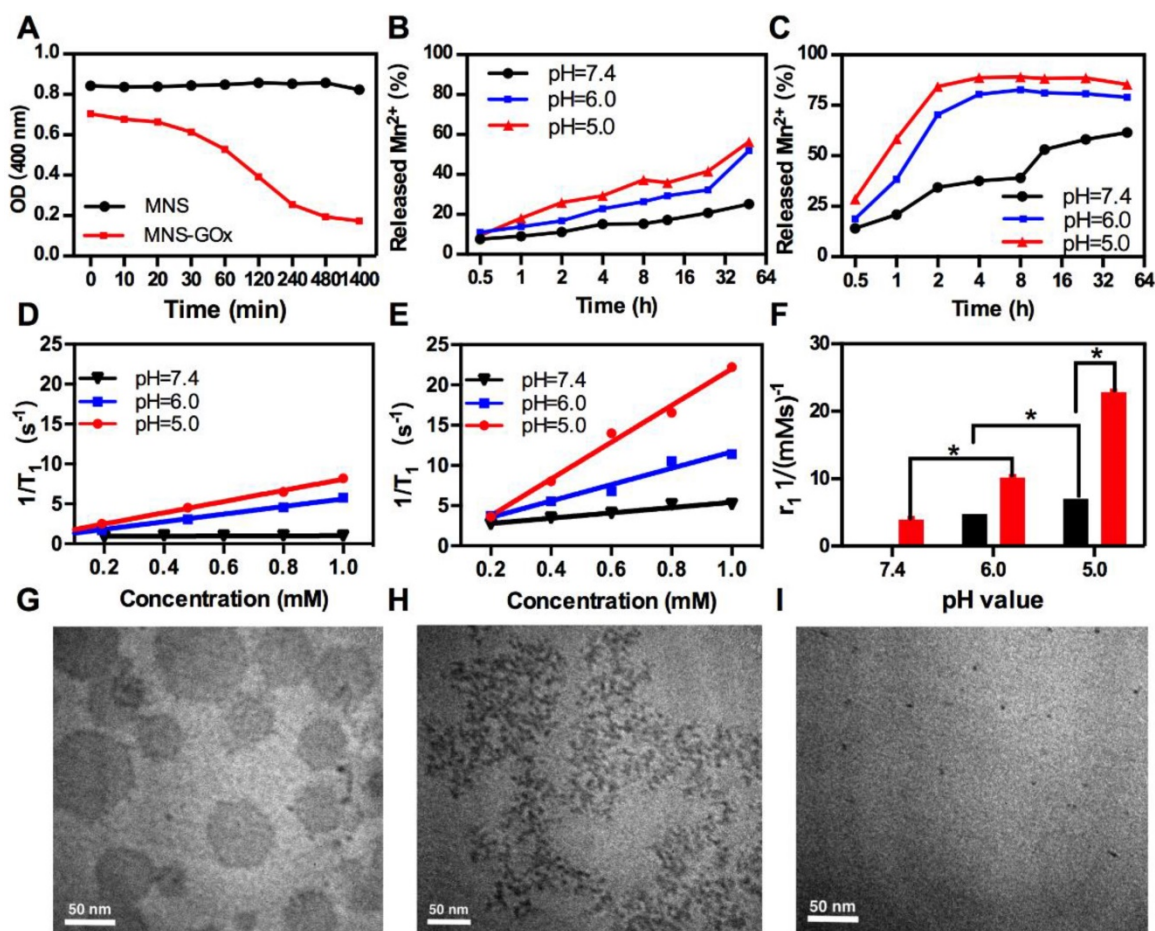


Figure 2. (A) The OD at 400 nm of MNS and MNS-GOx in PBS solutions (5 mM glucose, pH 7.4). The quantified concentration of Mn^{2+} released from MNS (B) or MNS-GOx (C) in PBS solutions (5 mM glucose, pH 5.0, 6.0, 7.4). The profile of $1/T_1$ vs Mn element concentration in MNS (D) and MNS-GOx (E) after 4 h incubation in PBS solutions (5 mM glucose, pH 5.0, 6.0, 7.4). (F) The corresponding T_1 relaxivity of MNS and MNS-GOx solutions. TEM images of MNS-GOx in PBS solutions (5 mM glucose, pH 7.4), before (G), 17 min (H), and 30 min (I).

electrons, Mn-based contrast agents have been widely explored as T_1 contrast agents. Based on the profile of $1/T_1$ vs Mn element concentration of MNS (Figure 2D) and MNS-GOx (Figure 2E), the $r_{1\text{MNS}}$ increased from 0.084 to 7.0 $\text{mM}^{-1}\text{s}^{-1}$ from pH 7.4 to 5.0, while $r_{1\text{MNS-GOx}}$ increased from 3.3 to 22.8 $\text{mM}^{-1}\text{s}^{-1}$ (Figure 2F). The $r_{1\text{MNS}}$ enhancement is due to the pH-responsive degradation of MNS, while the $r_{1\text{MNS-GOx}}$ enhancement is due to pH/glucose dual-responsive degradation of MNS, which accelerated the release of Mn^{2+} . In order to observe the degradation process of MNS-GOx, their morphology change was recorded by TEM imaging. As shown in Figure 2G-I, when MNS-GOx was incubated with 5 mM glucose, most of MNS was decomposed at 17 min, and no MNS can be found at 30 min. These results suggested MNS-GOx exhibited pH/glucose dual-responsive performance.

In vitro Synergistic Therapy

MnO_2 nanomaterials can catalyze the decomposition reaction of H_2O_2 to produce O_2 , which can promote the reaction of glucose oxidation¹⁶. As shown in Figure 3A, the glucose oxidation rate of

GOx and MNS-GOx were 2.69 and 3.43 mM/min , respectively. The catalytic activity enhancement of GOx by MNS can be attributed to the self-oxygenation of MNS-GOx during the glucose oxidation reaction that is an O_2 -dependent reaction. Afterwards, we investigated the catalytic activity of GOx at different temperature. The glucose concentrations were recorded by a glucometer, and extra O_2 was supplied into glucose solution for sufficient O_2 during the reaction. The results shown that V_{max} of MNS-GOx increased from $2.69 \times 10^3 \text{ M}/\text{min}$ at 30°C to $3.43 \times 10^3 \text{ M}/\text{min}$ at 50°C (Figure 3B). It was consistent with previous reports that the maximum activity of GOx at 50°C ^{40-41, 47-48}. Encouraged by the catalytic activity enhancement of GOx at high temperature, *in vitro* experiments were conducted on A375 cells for hyperthermia-enhanced synergistic therapy. MNS or MNS-GOx was incubated with A375 cells for 24 h, and then irradiation with or without 808 nm laser (1 W/cm^2 , 5 min). As shown in Figure 3C, cells incubated with MNS kept their viability over 81%. Cell viabilities of MNS + laser, MNS-GOx and

MNS-GOx + Laser groups showed concentration-dependent therapeutic effect. Importantly, MNS-GOx + laser group exhibited better therapeutic effect than that of MNS-GOx only. The synergistic therapeutic effect was further evidenced by live/dead cell staining (Figure 3D-F). No dead cells were found in control group (Figure 3D). For MNS + laser and MNS-GOx + laser groups, most of cells were dead in laser spots (Figure 3E-F). These results indicated the catalytic activity of GOx could be further improved by the hyperthermia of MNS-GOx upon 808 nm laser irradiation. Additionally, we assessed the catalytic activity of GOx before and after laser irradiation. As shown in Figure S9, the glucose reaction rates of MNS-GOx kept similar, which suggested the laser irradiation (808 nm, 1 W/cm², 5 min) can preserve the catalytic activity of GOx.

In Vivo Dual-Modal Imaging

MNS-GOx was composed of Mn element and melanin, which can be used as contrast agents for MRI and PAI, respectively. *In vivo* MR/PA dual-modal imaging was performed on the A375 tumor-bearing mice. MNS or MNS-GOx was intratumoral injected into A375 tumor-bearing mice at 5 mg/kg dose. Then the treated mice were scanned on 3T clinic MRI scanner. Both MNS and MNS-GOx displayed an obvious T₁-weighted enhancement in tumor tissues (Figure 4A). Compared with MNS treated mice, mice in MNS-GOx group exhibited stronger contrast effect

at each scan time point. Because MNS-GOx are pH/glucose dual-responsive, it can release more Mn²⁺ in tumor microenvironment than MNS, and the concentration of released Mn²⁺ will directly affect the longitudinal relaxivity and MRI contrast effect. So MNS-GOx group exhibited stronger contrast effect compared with MNS group. On the contrary to the increase of MR signal, PA signal of gradually decreased after injection over time (Figure 4B, Figure S10). As shown in Figure 4C, the quantified MR signal/noise ratio (SNR) of tumors treated with MNS-GOx gradually increased to the peak value of 2.67 at 8 h post-injection, while the SNR of tumors treated with MNS was only increased to 2.0 at 24 h post-injection. As shown in Figure 4D, the quantified PA signals of tumors treated with MNS or MNS-GOx gradually decreased over time. These results suggested MNS-GOx could achieve “turn-on” MR imaging and “turn-off” PA imaging simultaneously. MRI can offer high resolution contrast for soft tissue without tissue depth limits, but restricted by its poor sensitivity and time-consuming. PAI is convenient and time-saving possesses high optical imaging contrast, but limited imaging depth. So the dual-modal imaging can integrate different information to provide accurate diagnosis. A “turn on” MRI can light the deep tissues for precision cancer diagnosis, and the “turn off” PAI can monitor the treatment progress for individual treatment.

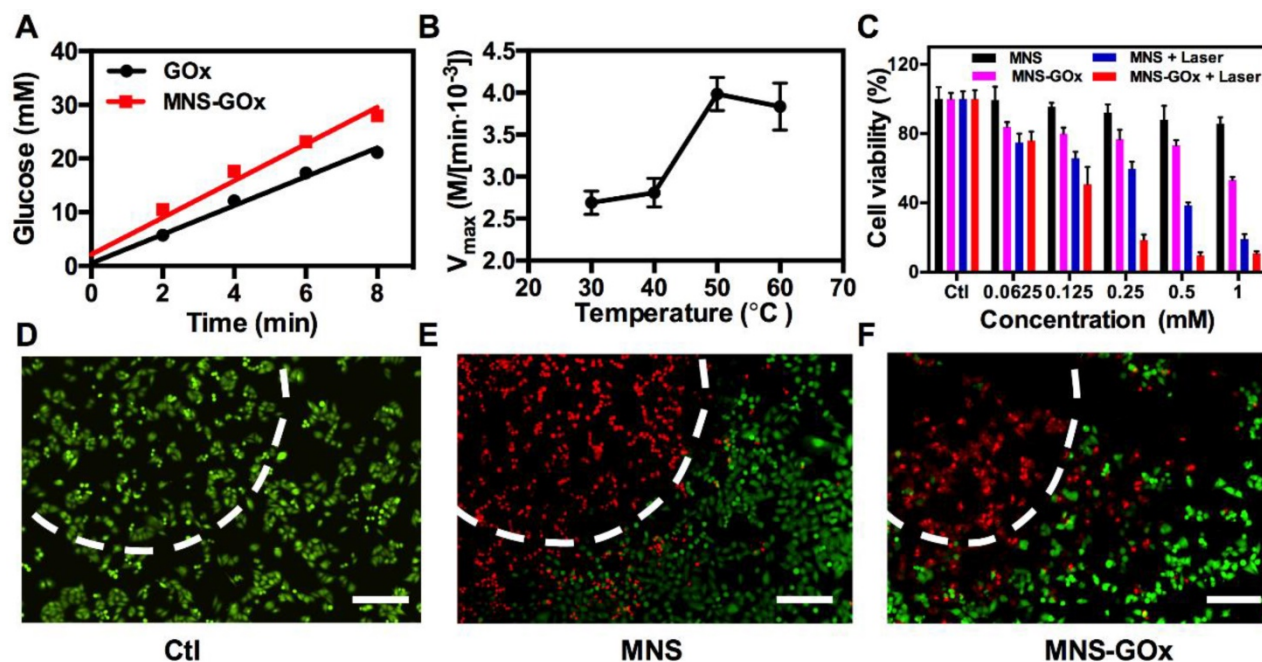


Figure 3. (A) The glucose oxidation rates of GOx and MNS-GOx at room temperature. (B) Kinetic parameters (V_{max}) of GOx obtained from the Michaelis–Menten plots at different temperatures. (C) A375 cell viability with four different treatments, including: control, MNS, MNS-GOx, MNS + laser, MNS-GOx + laser. Fluorescence images of Calcein AM (live cells, green fluorescence) and propidium iodide (PI) (dead cells, red fluorescence) co-stained A375 cells with different treatments, including control (D), MNS (E), MNS-GOx (F) (100 $\mu\text{g mL}^{-1}$) for 12 h with/without laser irradiation (808 nm, 1 W cm^{-2} , 5 min). Scale bar 100 μm .

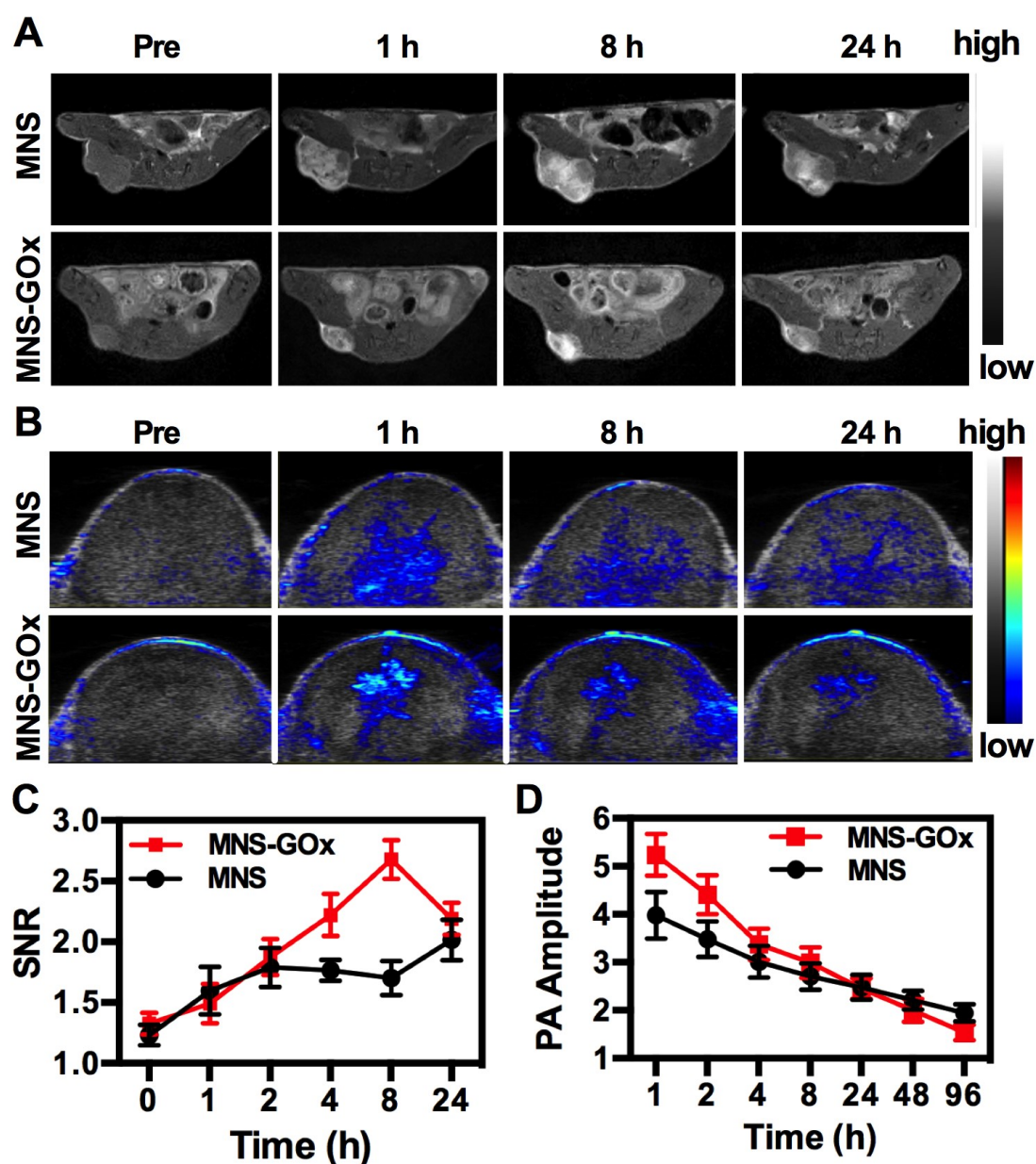


Figure 4. T₁-weighted MR (A) and PA images of mice treated with MNS or MNS-GOx at 0, 1, 8, 24 h post-injection. (C) The corresponding MR signal SNR analysis of tumor tissues in (A). (D) The corresponding PA signals of tumor tissues in (B).

In Vivo Synergistic Therapy

Based on *in vitro* synergistic PTT/starvation therapy effect, the *in vivo* synergistic therapy was conducted on A375 tumor-bearing mice. Mice were randomly divided into six groups: PBS, laser only, MNS, MNS+laser, MNS-GOx and MNS-GOx+laser. For all groups, the intratumoral injection dose was 5 mg/kg. For laser groups, 808 nm laser (0.6 W/cm², 5 min) was immediately irradiated on A375 tumor tissues after injection. The tumor volumes were measured every 2 days during 16 days. As shown in **Figure 5A**, the tumors of PBS and PBS + laser groups grew very fast, while MNS-GOx treated group shown

great suppression effect compared with MNS group. Interestingly, the tumors of MNS-GOx + laser group were completely eliminated; while MNS + laser group began to regrow at 10 days after treatment.

On the one hand, the increase of tumor local temperature upon laser irradiation can improve the catalytic activity of GOx, thus consuming more intratumoral glucose (~50 °C, **Figure S11**), on the other hand, MNS-GOx can perform the circular reaction of glucose oxidation and H₂O₂ decomposition for enhanced starvation therapy. The self-oxygenation/hyperthermia dually enhanced starvation cancer therapy shown higher tumor suppression effect than any single treatment.

Furthermore, the survival rate of mice in MNS-GOx group was greatly prolonged (**Figure 5B**). All treated mice had no obvious body weight change during different treatments (**Figure 5C**). The photographs of A375 tumor-bearing mice further evidenced the synergistic PTT/starvation effect (**Figure 5D**). Hematoxylin and eosin (H&E) staining images of tumor sections after treatments also indicated an obviously membrane fragmentation or shrinkage of nuclei in MNS + laser group and MNS-GOx + laser group (**Figure 5E**). But no significant damage or inflammation from H&E stained images of main organs (heart, liver, spleen, lung, kidney), negligible change of blood biochemistry results, and the hemolysis rates of various concentrations (15.5–400 $\mu\text{g/mL}$) of MNS were lower than 5.5% (**Figure S12–14**). These findings indicated that MNS-GOx exhibited a great potential in hyperthermia enhanced starvation synergistic therapy.

Conclusions

In summary, three different morphologies of MnO_2 nanomaterials were successfully synthesized by a biomimetic approach using melanin as a biotemplate at different pH conditions. Afterwards,

GOx loaded MnO_2 nanosheets (MNS) was explored as cancer nanotheranostics, especially for self-oxygenation/hyperthermia dually enhanced starvation therapy. The as-prepared MNS can decompose H_2O_2 to supply O_2 for the GOx catalyzed glucose oxidation reaction, thus promising the circular reaction of H_2O_2 decomposition and glucose oxidation. Moreover, the catalytic activity of GOx could be further improved by the hyperthermia of MNS-GOx upon NIR laser irradiation. Most intriguingly, MNS-GOx could achieve “turn-on” MR imaging and “turn-off” PA imaging simultaneously. The theranostic capability of MNS-GOx was evaluated both *in vitro* and *in vivo*. Finally, the as-prepared MNS-GOx exhibited pH/glucose dual-responsive performance, activatable MR/PA dual-modal imaging, and hyperthermia enhanced starvation synergistic cancer therapy, which provided a new nanoplatform for cancer nanotheranostics.

Supplementary Material

Supplementary figures.

<http://www.thno.org/v10p1544s1.pdf>

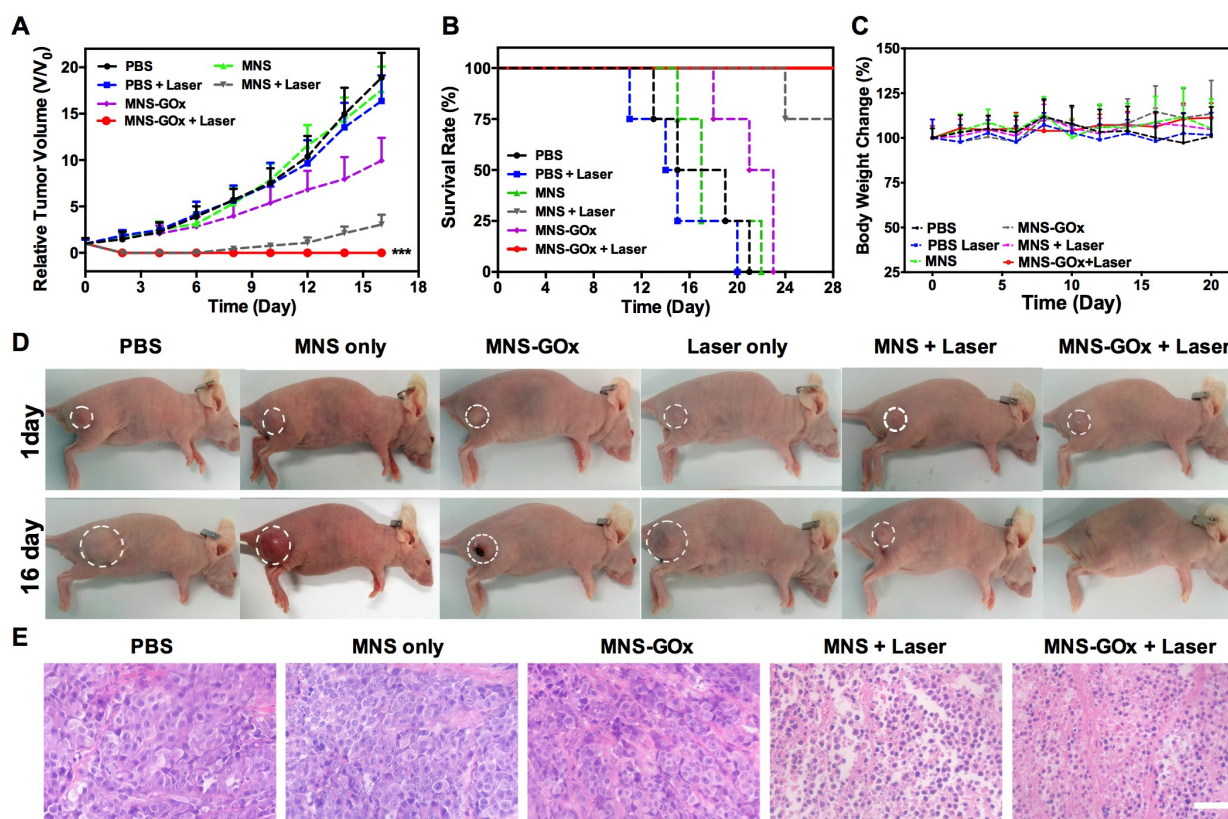


Figure 5. (A) Tumor growth curve, (B) survival curve and (C) body weight of A375 tumor-bearing mice (PBS, laser only, MNS, MNS+laser, MNS-GOx and MNS-GOx+laser) during the treatment process. (D) Digital photographs of A375 tumor-bearing mice of six groups after treatments. (E) H&E staining images of tumor sections harvested from A375 tumor-bearing mice (PBS, MNS only, MNS-GOx, MNS+laser and MNS-GOx+laser) after treatments. Scale bar: 100 μm . *** $p < 0.001$.

Acknowledgments

This work is financially supported by the Basic Research Program of Shenzhen (JCYJ20180507182413022), the National Natural Science Foundation of China (51573096, 51703132, 31771036), the National Key Research and Development Program (2018YFA0704003), the Guangdong Province Natural Science Foundation of Major Basic Research and Cultivation Project (2018B030308003), the Fok Ying-Tong Education Foundation for Young Teachers in the Higher Education Institutions of China (161032). We thank Instrumental Analysis Center of Shenzhen University (Lihu Campus).

Competing Interests

The authors have declared that no competing interest exists.

References

- Birsoy K, Possemato R, Lorbeer FK, et al. Metabolic determinants of cancer cell sensitivity to glucose limitation and biguanides. *Nature*. 2014; 508: 108-12.
- Wu D, Hu D, Chen H, et al. Glucose-regulated phosphorylation of tet2 by ampk reveals a pathway linking diabetes to cancer. *Nature*. 2018; 559: 637-41.
- Fan W, Lu N, Huang P, et al. Glucose-responsive sequential generation of hydrogen peroxide and nitric oxide for synergistic cancer starving-like/gas therapy. *Angew Chem Int Ed Engl*. 2017; 56: 1229-33.
- Fu LH, Qi C, Lin J, et al. Catalytic chemistry of glucose oxidase in cancer diagnosis and treatment. *Chem Soc Rev*. 2018; 47: 6454-72.
- Yu Z, Zhou P, Pan W, et al. A biomimetic nanoreactor for synergistic chemiexcited photodynamic therapy and starvation therapy against tumor metastasis. *Nat Commun*. 2018; 9: 5044-53.
- Zhao W, Hu J, Gao W. Glucose oxidase-polymer nanogels for synergistic cancer-starving and oxidation therapy. *ACS Appl Mater Inter*. 2017; 9: 23528-35.
- Chang K, Liu Z, Fang X, et al. Enhanced phototherapy by nanoparticle-enzyme via generation and photolysis of hydrogen peroxide. *Nano Lett*. 2017; 17: 4323-9.
- Li J, Dirisala A, Ge Z, et al. Therapeutic vesicular nanoreactors with tumor-specific activation and self-destruction for synergistic tumor ablation. *Angew Chem Int Ed Engl*. 2017; 56: 14025-30.
- Fu LH, Qi C, Hu YR, et al. Glucose oxidase-instructed multimodal synergistic cancer therapy. *Adv Mater*. 2019; 31: e1808325.
- Chu C, Su M, Zhu J, et al. Metal-organic framework nanoparticle-based biomineralization: A new strategy toward cancer treatment. *Theranostics*. 2019; 9: 3134-49.
- Zhang YF, Yang YC, Jiang SS, et al. Degradable silver-based nanoplatfor for synergistic cancer starving-like/metal ion therapy. *Mater Horiz*. 2019; 6: 169-75.
- Thews O, Wolloscheck T, Dillenburg W, et al. Microenvironmental adaptation of experimental tumours to chronic vs acute hypoxia. *Br J Cancer*. 2004; 91: 1181-8.
- Zheng X, Wang X, Mao H, et al. Hypoxia-specific ultrasensitive detection of tumours and cancer cells in vivo. *Nat Commun*. 2015; 6: 5834-46.
- Chen Q, Feng L, Liu J, et al. Intelligent albumin-MnO₂ nanoparticles as pH-/H₂O₂-responsive dissociable nanocarriers to modulate tumor hypoxia for effective combination therapy. *Adv Mater*. 2016; 28: 7129-36.
- Prasad P, Gordijo CR, Abbasi AZ, et al. Multifunctional albumin-MnO₂ nanoparticles modulate solid tumor microenvironment by attenuating hypoxia, acidosis, vascular endothelial growth factor and enhance radiation response. *ACS Nano*. 2014; 8: 3202-12.
- Yang X, Yang Y, Gao F, et al. Biomimetic hybrid nanozymes with self-supplied H⁺ and accelerated O₂ generation for enhanced starvation and photodynamic therapy against hypoxic tumors. *Nano Lett*. 2019; 19: 4334-42.
- Lin T, Zhao X, Zhao S, et al. O₂-generating MnO₂ nanoparticles for enhanced photodynamic therapy of bladder cancer by ameliorating hypoxia. *Theranostics*. 2018; 8: 990-1004.
- Fan W, Yung B, Huang P, et al. Nanotechnology for multimodal synergistic cancer therapy. *Chem Rev*. 2017; 117: 13566-638.
- Zhao Z, Fan H, Zhou G, et al. Activatable fluorescence/mri bimodal platform for tumor cell imaging via MnO₂ nanosheet-aptamer nanoprobe. *J Am Chem Soc*. 2014; 136: 11220-3.
- Lin LS, Song J, Song L, et al. Simultaneous fenton-like ion delivery and glutathione depletion by MnO₂-based nanoagent to enhance chemodynamic therapy. *Angew Chem Int Ed Engl*. 2018; 57: 4902-6.
- Gordijo CR, Abbasi AZ, Amini MA, et al. Design of hybrid MnO₂-polymer-lipid nanoparticles with tunable oxygen generation rates and tumor accumulation for cancer treatment. *Adv Funct Mater*. 2015; 25: 1858-72.
- Yang R, Hou M, Gao Y, et al. Biomineralization-inspired crystallization of manganese oxide on silk fibroin nanoparticles for in vivo MR/fluorescence imaging-assisted tri-modal therapy of cancer. *Theranostics*. 2019; 9: 6314-33.
- Pan W, Ge Y, Yu Z, et al. A cancer cell membrane-encapsulated MnO₂ nanoreactor for combined photodynamic-starvation therapy. *Chem Commun*. 2019; 55: 5115-8.
- Kim T, Cho EJ, Chae Y, et al. Urchin-shaped manganese oxide nanoparticles as pH-responsive activatable T₁ contrast agents for magnetic resonance imaging. *Angew Chem Int Ed Engl*. 2011; 50: 10589-93.
- Hu D, Chen L, Qu Y, et al. Oxygen-generating hybrid polymeric nanoparticles with encapsulated doxorubicin and chlorin e6 for trimodal imaging-guided combined chemo-photodynamic therapy. *Theranostics*. 2018; 8: 1558-74.
- Yang G, Xu L, Chao Y, et al. Hollow MnO₂ as a tumor-microenvironment-responsive biodegradable nano-platform for combination therapy favoring antitumor immune responses. *Nat Commun*. 2017; 8: 902-10.
- Shang J, Xie B, Li Y, et al. Inflating strategy to form ultrathin hollow MnO₂ nanoballoons. *ACS Nano*. 2016; 10: 5916-21.
- Chen Y, Ye D, Wu M, et al. Break-up of two-dimensional MnO₂ nanosheets promotes ultrasensitive pH-triggered theranostics of cancer. *Adv Mater*. 2014; 26: 7019-26.
- Chen JL, Li L, Wang S, et al. A glucose-activatable trimodal glucometer self-assembled from glucose oxidase and MnO₂ nanosheets for diabetes monitoring. *J Mater Chem B*. 2017; 5: 5336-44.
- Sheng J, Jiang X, Wang L, et al. Biomimetic mineralization guided one-pot preparation of gold clusters anchored two-dimensional MnO₂ nanosheets for fluorometric/magnetic bimodal sensing. *Anal Chem*. 2018; 90: 2926-32.
- Liu Z, Zhang S, Lin H, et al. Theranostic 2D ultrathin MnO₂ nanosheets with fast responsibility to endogenous tumor microenvironment and exogenous NIR irradiation. *Biomaterials*. 2018; 155: 54-63.
- Li B, Gu Z, Kurniawan N, et al. Manganese-based layered double hydroxide nanoparticles as a T₁-MRI contrast agent with ultrasensitive pH response and high relaxivity. *Adv Mater*. 2017; 29: 1700373-8.
- Meredith P, Sarna T. The physical and chemical properties of eumelanin. *Pigm. Cell Melanoma Res*. 2006; 19: 572-94.
- Longo DL, Stefania R, Aime S, et al. Melanin-based contrast agents for biomedical photoacoustic imaging and theranostic applications. *Int J Mol Sci*. 2017; 18: 1719-20.
- Lin J, Wang M, Hu H, et al. Multimodal-imaging-guided cancer phototherapy by versatile biomimetic theranostics with UV and gamma-irradiation protection. *Adv Mater*. 2016; 28: 3273-9.
- Zhang L, Sheng D, Wang D, et al. Bioinspired multifunctional melanin-based nanoliposome for photoacoustic/magnetic resonance imaging-guided efficient photothermal ablation of cancer. *Theranostics*. 2018; 8: 1591-606.
- Zhang YF, Bo SW, Feng T, et al. A versatile theranostic nanoemulsion for architecture-dependent multimodal imaging and dually augmented photodynamic therapy. *Adv Mater*. 2019; 31, e1806444.
- Zhang H, Liang X, Han L, et al. "Non-naked" gold with glucose oxidase-like activity: A nanozyme for tandem catalysis. *Small*. 2018; e1803256.
- Fan L, Lou D, Wu H, et al. A novel auno-based glucose oxidase mimic with enhanced activity and selectivity constructed by molecular imprinting and O₂-containing nanoemulsion embedding. *Adv Mater Interfaces*. 2018; 5: 1801070.
- Wang C, Zhang Q, Wang X, et al. Dynamic modulation of enzyme activity by near-infrared light. *Angew Chem Int Ed Engl*. 2017; 56: 6767-72.
- Golikova EP, Lakina NV, Grebennikova OV, et al. A study of biocatalysts based on glucose oxidase. *Faraday Discuss*. 2017; 202: 303-14.
- Ye Q, Zhou F, Liu W. Bioinspired catecholic chemistry for surface modification. *Chem Soc Rev*. 2011; 40: 4244-58.

43. Guo X, Chen S, Hu Y, et al. Preparation of water-soluble melanin from squid ink using ultrasound-assisted degradation and its anti-oxidant activity. *J Food Sci Tech Mys.* 2013; 51: 3680-90.
44. Park M, Lee N, Choi SH, et al. Large-scale synthesis of ultrathin manganese oxide nanoplates and their applications to T₁ MRI contrast agents. *Chem Mater.* 2011; 23: 3318-24.
45. Lim EK, Huh YM, Yang J, et al. pH-triggered drug-releasing magnetic nanoparticles for cancer therapy guided by molecular imaging by MRI. *Adv Mater.* 2011; 23: 2436-42.
46. Fan W, Bu W, Shen B, et al. Intelligent MnO₂ nanosheets anchored with upconversion nanoprobe for concurrent pH-/H₂O₂-responsive ucl imaging and oxygen-elevated synergetic therapy. *Adv Mater.* 2015; 27: 4155-61.
47. Kriaa M, Hammami I, Sahnoun M, et al. Purification, biochemical characterization and antifungal activity of a novel *aspergillus tubingensis* glucose oxidase steady on broad range of pH and temperatures. *Bioprocess Biosyst Eng.* 2015; 38: 2155-66.
48. Wu P, He Y, Wang HF, et al. Conjugation of glucose oxidase onto Mn-doped ZnS quantum dots for phosphorescent sensing of glucose in biological fluids. *Anal Chem.* 2010; 82: 1427-33.